On the interest of ground penetrating radar data for the estimation of unsaturated soil parameters

Moua Rohianuu [1], Lesparre Nolwenn [1], Girard Jean-François [1], Belfort Benjamin [1], Lehmann François [1], and Younes Anis [1]

[1]Université de Strasbourg, CNRS, ENGEES, EOST, ITES UMR 7063, F-67000 Strasbourg, France

Correspondence: Moua Rohianuu (rmoua@unistra.fr)

Abstract.

In this study, the interest of ground penetrating radar (GPR) time-lapse measurements for the estimation of hydrodynamic unsaturated soil parameters is investigated using synthetic infiltration experiments. Water movement and electromagnetic wave propagation in the unsaturated zone are modeled using a one-dimensional hydrogeophysical model. The GPR travel time data are analyzed for different reflectors: a moving reflector (the infiltration wetting front) and three fixed reflectors located at different depths in the soil. Global sensitivity analysis (GSA) is employed to assess the influence of the saturated hydraulic conductivity, the saturated and residual water contents, and the Mualem–van Genuchten shape parameters α and n of the soil on the GPR travel time data of the reflectors. Statistical calibration of the soil parameters is then performed using the Markov chain Monte Carlo (MCMC) method. The impact of the type of reflector (moving or fixed) is then evaluated by analyzing the calibrated model parameters and their confidence intervals for different scenarios. GSA results show that the sensitivities of the moving and fixed reflectors data to the hydrodynamic soil parameters are different whereas the fixed reflectors have similar sensitivities. Results of parameter estimation show that the use of only data from the moving or fixed reflectors does not allow a good identification of all soil parameters. When both data are combined, all soil parameters can be well estimated with narrow confidence intervals.

Keywords: coupled hydrogeophysical model; time-lapse ground penetrating radar; unsaturated soil parameters; global sensitivity analysis; Bayesian parameter estimation; uncertainty quantification.

1 Introduction

The vadose zone is defined by the region between the ground surface and the groundwater table. Because of its location, it is at the center of the interactive atmospheric-surface-underground water system. Hence, understanding water flow in the vadose zone is crucial for hydrological modeling and forecasting that can be useful for water resources management, agricultural practices optimization, or geotechnical studies. The porous medium in the vadose zone is filled by both water and air phases. The air phase is considered infinitely mobile and remains at atmospheric pressure. The movement of water has a non-linear behavior and is characterized by two fundamental hydraulic relationships, namely the water retention and the hydraulic con-

25 ductivity functions. Various mathematical expressions can describe these functions in terms of dependent variables and fitting parameters. In this work, we use the Mualem-van Genuchten (Mualem 1976, van Genuchten 1980) hydraulic conductivity and water retention models. These models include the following unsaturated soil hydraulic parameters: the saturated hydraulic conductivity, the saturated and residual water contents, and the Mualem–van Genuchten shape parameters α and n.

Different approaches can be applied to estimate the unsaturated soil parameters. A typical and prevalent approach relies
30 on laboratory measurements conducted on soil core samples. The typical measurement approaches can be of various types but common practices rely on hydraulic fluxes measurements (Vereecken et al., 2008). If this approach can be accurate at the column scale, it is prone to certain limitations when the objective is to deduce the soil parameter values at larger scales. Indeed, sample analysis through laboratory experiments is unlikely to provide parameter estimates at field conditions since the volume of the analyzed samples is often not representative of the field heterogeneity at the mesoscale (Scharnagl et al.,
35 2011). In addition, the method is invasive and can be labor-intensive for deep or large scales investigations (Binley et al., 2015). Furthermore, the conservation of collected samples can be challenging because of issues of compaction and changes in porosity.

A more appropriate approach for large scales is based on the monitoring of underground water content. In fact, water content measurements can show significant variations because of their sensitivity to different hydrological processes. As a
40 consequence, they are convenient for the estimation of soil parameters of the subsurface at the field scale by inverse modeling. Water content measuring techniques can be classified into two categories, based on whether they provide information on water content directly or not. The first group uses direct measurements conducted at the point scale with water content sensing techniques, for instance using thermal or electromagnetic sensors (e.g., capacitance or time domain reflectometry, Jones et al., 2005; Belfort et al., 2019). These techniques can yield data with great resolution at one location and give information on the
45 dynamics at the field scale (Vereecken et al., 2008). In addition, measurements taken at various locations can help to describe the distribution of water content, and thus, allow a good characterization of the state of the soil. However, the installation of sensors is often laborious, time-consuming, and destructive (Huisman et al., 2003; Dal Bo et al., 2019). Furthermore, their reliability requires an accurate calibration (Robinson et al., 2008).

The second category uses indirect measurements of the water content, like remote sensing and hydrogeophysical methods
50 with non-invasive devices. Remote sensing techniques use devices that are not in direct contact with the ground, such as unmanned aerial vehicles thermal infrared imagery (Zhang et al., 2019) or airborne ground penetrating radar (Edemsky et al., 2021). These methods provide the mapping of water content at a large scale and in locations where direct sensing measurements cannot be conducted. However, remote sensing methods exhibit a penetration depth of only a few centimeters and are often limited by the vegetation density (Vereecken et al., 2008; Robinson et al., 2008).

55 Common hydrogeophysical methods include electromagnetic induction (Doolittle and Brevik, 2014), direct current resistivity (de Jong et al., 2020), nuclear magnetic resonance (Costabel and Günther, 2014), and ground penetrating radar (GPR) (Huisman et al., 2003; Klotzsche et al., 2018) methods. These techniques supply indirect information on hydraulic properties or states, at various scales, from estimated geophysical properties. As mentioned by Binley et al. (2015), such conversion from

geophysical to hydraulic properties or states requires the use of robust petrophysical relationships to provide reliable estimates
60   of hydraulic parameters.

Nowadays, GPR is highly used in the field of hydrogeophysics. Different techniques have been reviewed and discussed by
Huisman et al. (2003) and Klotzsche et al. (2018). GPR is highly sensitive to water content, and, as such, it can close the gap
between the spatial scales covered by direct and remote sensing techniques. Furthermore, the temporal variability of the soil
water content can be characterized from time-lapse measurements. For instance, GPR data can be collected during artificial
65   experiments (e.g., infiltration, runoff, drainage, imbibition) that can provide interesting information on the flow characteristics
(e.g., Saintenoy et al., 2008; Moysey, 2010; Scholer et al., 2011; Busch et al., 2013; Jonard et al., 2015; Jaumann and Roth,
2018; Léger et al., 2014; 2016; 2020). Note however that the hydraulic properties estimated from GPR data are subject to an
inherent compromise between a deep investigation and a fine spatial resolution. For instance, the lowest frequencies (typically
from 1 GHz down to 100 MHz) allow deeper penetrations (until a maximum depth between 1 m and 3 m in most organic
70   media).

Saintenoy and Hopmans (2011) performed a sensitivity analysis to evaluate the importance of the soil parameters on the
reflections caused by the water table. They found that the detectability of the GPR reflections is mainly dependent on the
slope of the retention curve in the capillary zone. Moysey (2010) showed that the Mualem-van Genuchten parameter n is the
most poorly constrained among all unsaturated soil parameters when considering the two-way travel time (TWT) from various
75   sources of reflection for a laboratory infiltration experiment conducted in a sandbox. At the laboratory scale, Léger et al. (2020)
have monitored imbibition-drainage experiments using a single-offset surface GPR. At the field scale, infiltration experiments
have been monitored with a single-offset surface GPR (Léger et al., 2014; 2016) or off-ground GPR (Jadoon et al., 2012). Saito
et al. (2018) used a more complex multi-offset and multi-channel surface GPR to directly monitor the wetting front progression.
Mono-channel multi-offset technique is usually not suited for monitoring experiments with high temporal variability, as the
80   offset must be adjusted between each measurement. The multi-channel technique has the advantage to be multi-offset and is,
therefore, able to simultaneously determine the propagation speed and the depths of reflectors.

Time-lapse GPR monitoring of artificial infiltrations is one of the cheapest non-destructive methods that can be easily
conducted to estimate the unsaturated soil parameters in field conditions. Léger et al. (2014) have demonstrated the relevance
of such a methodology to evaluate the hydraulic parameters of sandy soil. The authors have investigated synthetic and field
85   examples and showed that the inverted parameters were in agreement with the values obtained in the laboratory for soil samples
and with disk infiltrometer measurements. However, in their study, Léger et al. (2014) didn't assess the reliability of the
estimated values since the uncertainty associated with the calibrated parameters has not been evaluated. Furthermore, Léger et
al. (2014) employed only the TWT data obtained from the GPR reflection on the wetting front for the calibration of the soil
parameters. The present study extends the work of Léger et al. (2014) by:

90   – Considering different reflectors at different depths: a moving reflector which corresponds to the infiltration dynamic
         wetting front and two fixed reflectors located at different depths in the soil.

- Investigating the influence of all soil parameters (the saturated hydraulic conductivity, the saturated and residual water contents, and the Mualem–van Genuchten shape parameters α and n) on the GPR TWT data of the three reflectors using Global Sensitivity Analysis (GSA).

95 - Performing statistical calibration of soil parameters using the Markov Chain Monte Carlo (MCMC) method and evaluating the reliability of the estimated parameters by analyzing not only the calibrated model parameters but also their associated uncertainty.

- Evaluating the impact of the type of reflector (moving or fixed) by analyzing the calibrated model parameters and their confidence intervals for different scenarios.

100 The plan of the paper is as follows: Section 2 describes the test case as well as the mathematical and numerical hydrogeophysical models. Section 3 reports on the GSA results of the different TWT signals. Then, Section 4 discusses the results of soil parameter estimation with MCMC for different scenarios.

2 Test case description and numerical solution

2.1 Test case description

105 The test case considered in this work is a hypothetical one-dimensional experiment of water infiltration in a homogeneous sandy soil of 150 cm (Fig.1a). The infiltration is driven by a constant pressure head of 10 cm applied at the surface of the soil (i.e., a 10 cm water ponding condition is maintained at the top). The medium is initially at the hydrostatic equilibrium with a water table maintained at 100 cm below the soil surface (Fig.1b). The domain is initially formed by an unsaturated zone of 100 cm thick above a saturated zone of 50 cm thick. We assume the experiment to be monitored with a surface GPR.

110 The propagating time (i.e., the TWT) of the GPR waves reflected by two types of reflectors are considered (Fig.1c): (i) the moving infiltration wetting front and (ii) two fixed reflectors corresponding to a local heterogeneity at two different depths. For instance, these can be small objects that are artificially buried (e.g., moisture sensing probes) or naturally embedded (such as small rocks) in the porous medium. The fixed reflectors are supposed to be small enough compared to the section of the infiltrated area, so they do not significantly perturb the vertical flow. The upper fixed reflector, R50, is located in the initially

115 unsaturated zone at 50 cm depth. The reflector R120 is located in the saturated zone, under the water table, at a distance of 120 cm from the soil surface (Fig.1a). In the following, the time-lapse TWT signal for reflection caused by the infiltration wetting front is noted TWT_f and that from the two immovable diffracting points R50 and R120, are respectively noted TWT_{50} and TWT_{120}.
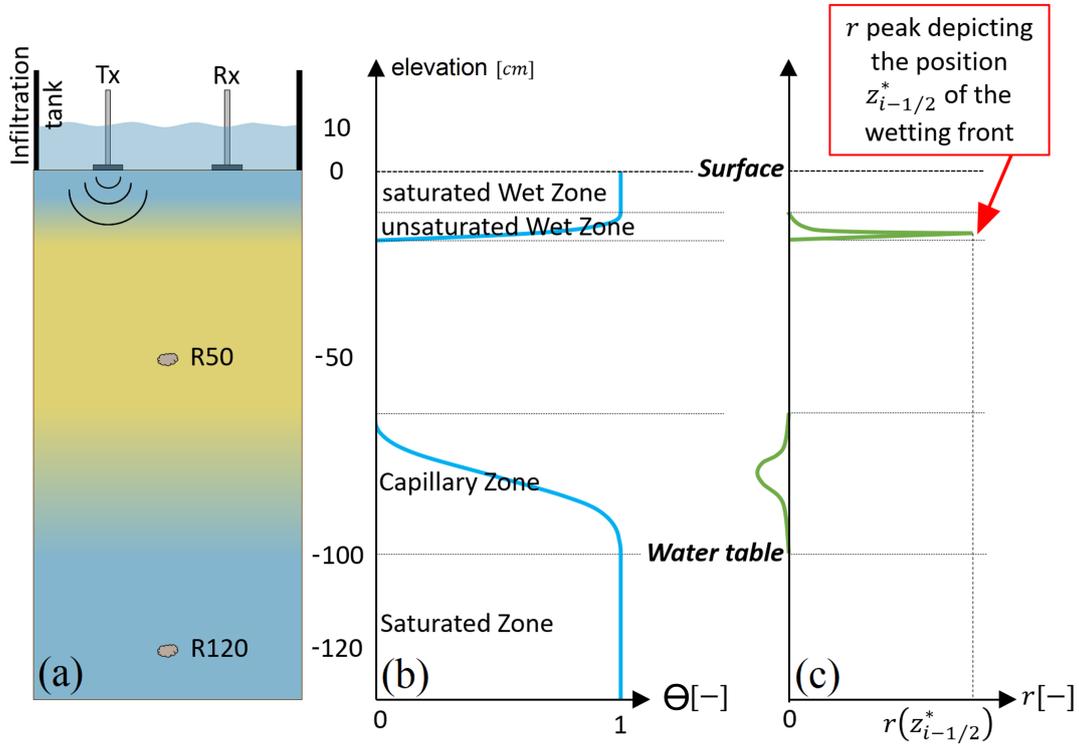
Figure 1. Test case and experimental device illustration at an advanced time step (a). R50 and R120 are fixed reflectors considered in this experiment. TX and RX refer to the transmitter and receiver antennas of the GPR system. Effective saturation S_e (b) and reflection coefficient r (c) profiles with depth.

2.2 The mathematical model

120 ### 2.2.1 Unsaturated flow model

Water infiltration in unsaturated/saturated soils is governed by the one-dimensional Richards' equation (Richards, 1931):

$$\frac{\partial \theta}{\partial t} = \frac{\partial}{\partial z}\left[K(\theta)\left(\frac{\partial h}{\partial z} - 1\right)\right] \tag{1}$$

where h (cm) is the pressure head; z is the depth (cm), taken positive in the downward direction; t is the time (s), θ (cm³/cm³) is the actual water content, and $K(\theta)$ (cm/s) is the hydraulic conductivity which is a function of water content. The initial

125 condition is a hydrostatic pressure distribution corresponding to a water table at 100 cm depth. The boundary condition at the top of the domain is a fixed Dirichlet condition of 10 cm maintained during the experiment. The boundary condition at the bottom is a piezometric head fixed at -100 cm which corresponds to the water table position (Fig.1).

The interdependencies of the pressure head, conductivity, and water content are described using the standard models of Mualem (1976) and van Genuchten (1980):

$$S_e(h) = \frac{\theta(h) - \theta_r}{\theta_s - \theta_r} = \begin{cases} [1 + (\alpha|h|)^n]^{-m} & \text{if } h < 0 \\ 1 & \text{if } h \geq 0 \end{cases} \tag{2}$$

$$K(h) = \begin{cases} K_s \times S_e(h)^{1/2}[1 - (1 - S_e(h)^{1/m})^m]^2 & \text{if } h < 0 \\ K_s & \text{if } h \geq 0 \end{cases} \tag{3}$$

where $S_e(h)$ (-) is the effective saturation, θ_s and θ_r (cm^3/cm^3) are the saturated and residual water contents respectively, K_s (cm/s) is the saturated conductivity, $m = 1 - 1/n$, α (1/cm) and n (-) are the Mualem-van Genuchten shape parameters.

2.2.2 Petrophysical and Geophysical relationships

In GPR sounding, pulses of radiofrequency (MHz to GHz) electromagnetic waves are emitted from a transmitting antenna through the sounded medium. The electromagnetic response is then acquired with a receiving antenna. With a surface GPR, both antennas are installed at the surface of the soil Fig.1). To monitor the experiment of water infiltration with time-lapse GPR, the sounding system is set immobile above the infiltration zone in order to capture the time variation of the electromagnetic response due to the change of saturation.

To describe the dependency of the dielectric permittivity on the water content, we use the complex refractive index model (Birchak et al., 1974). This petrophysical relationship relates the dielectric constant ϵ (-) of a three-phase (water-solid-air) medium to its water content by:

$$\sqrt{\epsilon(z,t)} = \theta(z,t)\sqrt{\epsilon_w} + (1 - \phi)\sqrt{\epsilon_s} + [\phi - \theta(z,t)]\sqrt{\epsilon_a} \tag{4}$$

where ϕ (-) is the porosity, $\epsilon_w = 80$, $\epsilon_s = 2.5$ and $\epsilon_a = 1$ are the relative dielectric constants of water, silica (sand) and air, respectively.

In a low electrical conductivity and non-magnetic soil, the electromagnetic waves propagate at a speed V (cm/ns) (Annan, 2003):

$$V = \frac{c}{\sqrt{\epsilon}} \tag{5}$$

where $c \approx 30$ cm/ns is the speed of electromagnetic waves in air, and ϵ (-) is the dielectric constant of the porous medium. Equations (4) and (5) evidence that GPR waves propagate at a much lower speed in wet conditions. Any source of reflection in the sounded soil produces a reflected wave that is recorded at a time corresponding to the duration of its propagation, from the transmitting antenna, down to the source of reflection, then back up to the receiving antenna, i.e., the TWT of the reflected

wave.

We consider a one-dimensional scenario (the offset between the antennas is null) and discretize the domain into N cells i, centered at a depth z_i, with element boundaries at $z_{i-1/2}$ and $z_{i+1/2}$. The TWT for the reflection occurring at the interface $(i-1/2)$ between the elements $i-1$ and i can be expressed as the sum of the vertical TWT in each element above i:

160
$$\text{TWT}(z_{i-1/2}) = 2 \sum_{j=1}^{i-1} \frac{|l_j|}{V_j} \tag{6}$$

in which $|l_j|$ (cm) is the length of the element j above i and V_j (cm/ns) is the GPR propagation speed in the element j.

A reflection occurs at the interface between two successive elements if the reflection coefficient is not zero. The reflection coefficient expresses the contrast of dielectric constant (due to the contrast of water content) at the interface between the two elements $i-1$ and i. When the offset between transmitting and receiving antennas is null, the reflection coefficient at interface

165 $(i-1/2)$ is defined by:

$$r(z_{i-1/2}) = \frac{\epsilon(z_i) - \epsilon(z_{i-1})}{\epsilon(z_i) + \epsilon(z_{i-1})} \tag{7}$$

where $\epsilon(z_i)$ is the dielectric constant of the element i.

For an 800 MHz antenna, the wavelength can typically vary from 6 cm in a wet medium to around 18 cm in a dry medium. The abrupt change in the reflection coefficient makes the wetting front easily detectable whatever the hydraulic parameters,

170 contrarily to the water table which may be hidden due to the capillary fringe (Bano, 2006; Saintenoy and Hopmans, 2011).

2.3 The numerical model

The variation of the water content in the soil during the infiltration is computed using the WAMOS-1D code (Belfort et al., 2018). The model describes the water movement in the porous medium using Richards' equation (1), and the constitutive relationships between the pressure, the hydraulic conductivity, and the volumetric water content given by Eq. (2) and Eq. (3).

175 The domain of 150 cm depth is discretized with uniform elements of 1 cm thick with homogeneous properties. The WAMOS-1D code solves the system of Eqs. (1)-(3) and yields the vertical distribution of water content at each time step. This distribution is then converted into a vertical dielectric permittivity profile ϵ using the petrophysical relationship Eq. (4) and into a GPR wave propagation speed profile V using Eq. (5). Then, the time-lapse TWT signals for the fixed objects, TWT_{50} and TWT_{120}, are calculated at each time step using Eq. (6) (dashed and dotted curves in Fig.2).

180 The time-lapse signal TWT_f, induced by wave reflection on the wetting front because of the sharp water content variation at the front position is calculated in two steps. First, we search the wetting front position $z^*_{i-1/2}$, which corresponds to the interface position having the maximum reflection coefficient from Eq. (7) as illustrated in Fig.1. Then, the TWT signal of the wetting front is obtained using $\text{TWT}_f = \text{TWT}(z^*_{i-1/2})$ from Eq. (6) (solid curve Fig.2).

Note that TWT_{50} and TWT_{120} signals are induced by fixed objects, thus, these signals exist regardless of the position of

185 the infiltration front. On the other hand, TWT_f is induced by the infiltration wetting front whose position varies over time. Besides, contrarily to TWT_{50}, and TWT_{120}, the TWT_f signal disappears when the wetting front reaches the water table. To
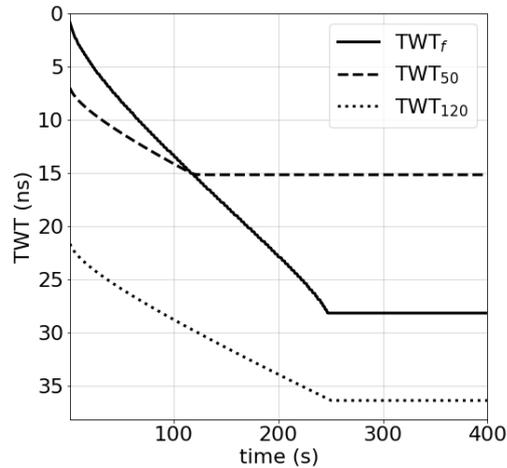
Figure 2. Hydrogeophysical model responses for $K_s = 0.08$ cm/s, $\theta_s = 0.4$ (-), $\theta_r = 0.07$ (-), $\alpha = 0.145$ cm^{-1}, $n = 2.68$ (-). TWT$_f$ corresponds to the TWT signal for the wetting front, while TWT$_{50}$ and TWT$_{120}$ are the TWT signals for fixed objects located at 50 and 120 cm below the surface, respectively.

avoid numerical issues when simulations are performed with different soil parameter sets, the value of TWT$_f$ when the water table is reached, is artificially maintained for the remaining time steps until the end of simulation time. The water table is assumed to be reached when the maximum reflection coefficient of Eq. (7) is under a threshold of 10^{-2}. This reflects a fully

190   saturated domain with an almost uniform water content distribution (solid curve Fig.2). An explanation of the computation of all TWT signals is summarized in Fig.3.

3 Global sensitivity analysis of TWT signals

3.1 GSA method

The GSA method evaluates how the outputs of a model are influenced by the variation of the input parameters (Mara and

195   Tarantola, 2008). Among the various forms of GSA, a variance-based sensitivity analysis, allowing the calculation of Sobol sensitivity indices (Sobol′, 2001) is employed. Such indices depict the contribution of the variation of any input variable x to the total variance of an output variable y. In our case, the input variables are the unsaturated soil parameters (K_s, θ_s, θ_r, α, n) and the output variables are the TWT signals (TWT$_f$, TWT$_{50}$, TWT$_{120}$).

Given a model with a set of p independent random parameters $\boldsymbol{X} = \{x_1, x_2, ..., x_p\}$ that yields a random response $y(\boldsymbol{X})$,

200   the two variance-based sensitivity measures, also called Sobol indices (Sobol′, 2001) are:
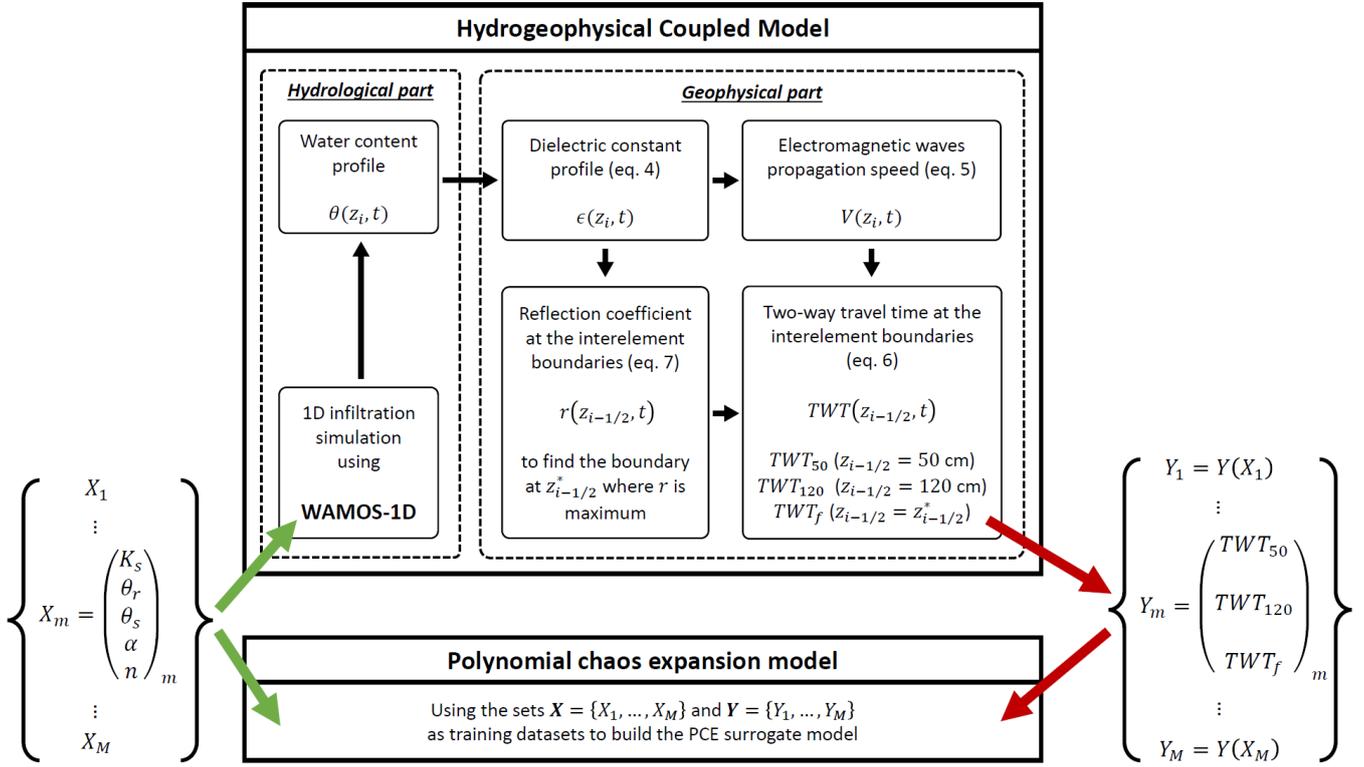
Figure 3. Summary of the working process of the forward hydrogeophysical model and how it is used to build the PCE surrogate model.

– the first-order sensitivity index:

$$S_i = \frac{\text{Var}\left[E\left[y(\boldsymbol{X})|x_i\right]\right]}{\text{Var}\left[y(\boldsymbol{X})\right]} \in [0,1] \tag{8}$$

– the total sensitivity index:

$$ST_i = \frac{E\left[\text{Var}\left[y(\boldsymbol{X})|x_{-i}\right]\right]}{\text{Var}\left[y(\boldsymbol{X})\right]} \in [0,1] \tag{9}$$

where $x_{-i} = \boldsymbol{X} \setminus x_i$ is the set of all parameters except x_i, $E()$ and $E(.|.)$ are respectively the expectation and the conditional expectation operators, $\text{Var}()$ and $\text{Var}(.|.)$ are the variance and the conditional variance, respectively. The first-order index S_i quantifies the contribution of the parameter x_i alone to the total variance of $y(\boldsymbol{X})$, while ST_i also includes all interactions of x_i with the other parameters x_{-i}.

To perform a variance-based GSA, a practical approach (to save computational time) is to use Polynomial Chaos Expansion (PCE; Wiener, 1938). The PCE approach consists in developing any signal $y(\boldsymbol{X})$ as a set of orthonormal multivariate polynomials of a degree not exceeding D:

$$y(\boldsymbol{X}) = \sum_{|\beta| \leq D} s_\beta \Psi_\beta(\boldsymbol{X}) \tag{10}$$

	K_s (cm/s)	θ_s (cm^3/cm^3)	θ_r (cm^3/cm^3)	α (1/cm)	n (-)
$[x_{\min} - x_{\max}]$	[0.001 - 0.15]	[0.32 - 0.48]	[0.01 - 0.13]	[0.01 - 0.28]	[1.5 - 10]

Table 1. Prior intervals of the unsaturated soil parameters for both GSA and Bayesian estimation.

	TWT$_f$	TWT$_{50}$	TWT$_{120}$
$t = 50$ s			
Var_HYD_model	14	5	15.9
Var_PCE_model	13.4	5	15.8
Var_error	4.3%	0.9%	0.5%
$t = 150$ s			
Var_hyd_model	54.6	5.5	23.3
Var_PCE_model	53.9	5.4	23.2
Var_error	1.3%	1.4%	0.4%
$t = 2000$ s			
Var_hyd_model	28.8	1.5	9.9
Var_PCE_model	27.1	1.4	9.3
Var_error	5.7%	7.4%	5.2%

Table 2. Variance of TWT$_f$, TWT$_{50}$ and TWT$_{120}$ signals at $t = 50$ s, 150 s and 2000 s calculated with the PCE surrogate model and with the hydrogeophysical model.

where $\beta = \beta_1, \beta_2, ..., \beta_p \in \mathbb{R}^p$ is a pth–dimensional index, s_β are the PC coefficients, Ψ_β are the generalized polynomial chaos of degree $|\beta| = \sum_{i=1}^p \beta_i$.

215   In this work, Legendre polynomials are used since uniform distributions are assumed for all uncertain parameters. Uniform distributions express the absence of prior information. This makes all parameter values in the given prior intervals equally likely. Large prior distribution intervals are considered for all unsaturated soil parameters (Table 1).

The number of coefficients for a full PCE representation is $P = (p + D)!/p!D!$. A training dataset of M realizations of the forward coupled hydrogeophysical model is used to build the PCE surrogate model of order D (Fajraoui et al, 2011; Shao et

220   al., 2017; Younes et al., 2013). The coefficients of the PCE are obtained by searching the best fit (in the least square sense) of the PCE surrogate model to the hydrogeophysical model for the M realizations. To work with low-discrepancy sets, the M realizations correspond to sets of input parameters sampled from their prior probability distributions, using quasi-random Sobol sequences (Shao et al., 2017). We illustrate the principle of the construction of the PCE with our hydrogeophysical model in Fig.3.

225   A PCE is constructed at each time step for all model responses (TWT$_f$, TWT$_{50}$, and TWT$_{120}$) since we deal with transient simulations. In this work, $M = 2048$ hydrogeophysical model realizations are employed to obtain PCEs of degrees $D = 5$ containing $P = 252$ coefficients. The obtained PCEs are sufficiently accurate as the variance of the TWT output signals is calculated with the surrogate PCE model and the forward hydrogeophysical model at three different times $t = 50$ s, 150 s, and 2000 s. The results of Table 2 show that the relative difference between the two variances is very small for all investigated times.

230   Note that although the relative variance error for the TWT$_{50}$ at $t = 2000$ s is the largest (around 7%), it remains insignificant since the total variance of the signal at this time is negligible (less than 2 ns^2). The variance of the forward hydrogeophysical model is therefore well reproduced by the PCE surrogate model which will be employed for the GSA of the TWT signals using the variance decomposition.

3.2   GSA results

235   The temporal distribution of the output variance of the three TWT signals (TWT$_f$, TWT$_{50}$ and TWT$_{120}$) are represented Fig.4. For each TWT signal, the variance is represented by the black curve and the relative contributions of the uncertain parameters to the variance are represented by the shaded area. The blank region between the variance curves and the shaded area represents interactions between parameters.

TWT$_f$ has a different behavior from the TWT signals of fixed reflectors TWT$_{50}$ and TWT$_{120}$ (Fig.4). Although the TWT

240   signals of fixed reflectors have different variance magnitudes, they exhibit similar behavior (Fig.4b and 4c). The variance of the TWT signal is five times more significant for TWT$_{120}$ than for TWT$_{50}$. This is in agreement with the physics since the zone of the porous medium affecting the GPR wave is more important for the TWT$_{120}$ signal than for the TWT$_{50}$. In addition, the period of influence of the unsaturated parameters (θ_r, α, n) is also more important for TWT$_{120}$ than for TWT$_{50}$ since saturated conditions for the reflector R120 are reached much later than for R50. Since fixed reflectors exhibit similar behavior, in the

245   following, we comment on the results of TWT$_f$ and TWT$_{120}$ signals.

3.2.1   GSA of the TWT$_f$ signal

TWT$_f$ variance is zero at the beginning of the infiltration (Fig.4a) which means that the TWT$_f$ signal is not affected by the initial conditions. Indeed, the infiltration wetting front and the TWT$_f$ signal start at zero for all parameter sets. Then, the variance of the signal increases until a maximum of 60 ns^2, reached at around 3 min. After that, the variance decreases, but

250   keeps a significant value of around 25 ns^2 (Fig.4a). Concerning parameter sensitivities, at the beginning, the TWT$_f$ signal is mainly affected by K_s. The influence of this parameter decreases over time and reaches zero for long times when steady-state conditions (corresponding to a fully saturated soil) are reached. The parameter θ_s has a moderate influence on the TWT$_f$ signal. Its influence is not observable at short times since unsaturated conditions occur. Overall, the most influential parameter on the TWT$_f$ signal is the van Genuchten parameter α. This parameter seems influential even for saturated conditions. Note that this

255   numerical artifact is observed because the value of TWT$_f$ is artificially maintained when the infiltration wetting front reaches the water table, while physically the signal disappears. The effects of the parameters θ_r and n are not observable (Fig.4a). The blank region between the variance curve and the shaded area in this figure is due to the interaction between the parameters.
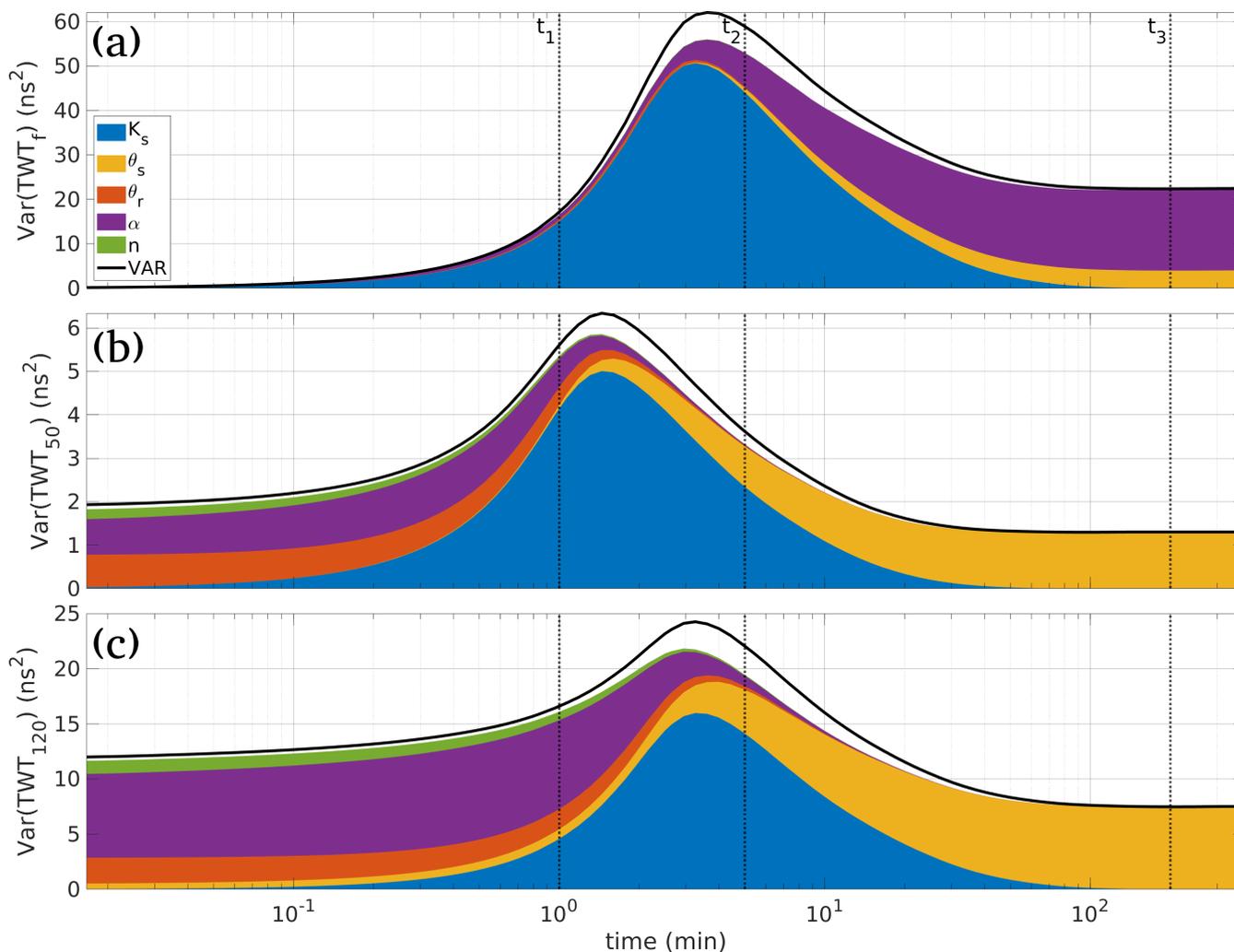
Figure 4. Time distribution of the variance of TWT_f (a), TWT_{50} (b) and TWT_{120} (c). The shaded area under the variance curve represents the partial marginal contributions of the uncertain parameters; the blank region between the shaded area and the variance curves represents the contribution of interactions between the parameters. The marginal effects shown in Fig.6 are represented at three time steps $t_1 = 1$ min, $t_2 = 5$ min, and $t_3 = 200$ min, highlighted here (dotted black lines).

To estimate this interaction, we plot the difference between the total (ST_i) and the first order (S_i) sensitivity indices for all parameters (Fig.5a). This difference reflects the interaction between the parameters over time. Interactions between parameters are negligible for all parameters ($ST_i \approx S_i$), except for K_s and α (Fig.5a). Hence, the interaction between these two parameters affects the variance of the TWT_f signal as represented by the blank region between the variance curve and the shaded area (Fig.4a).
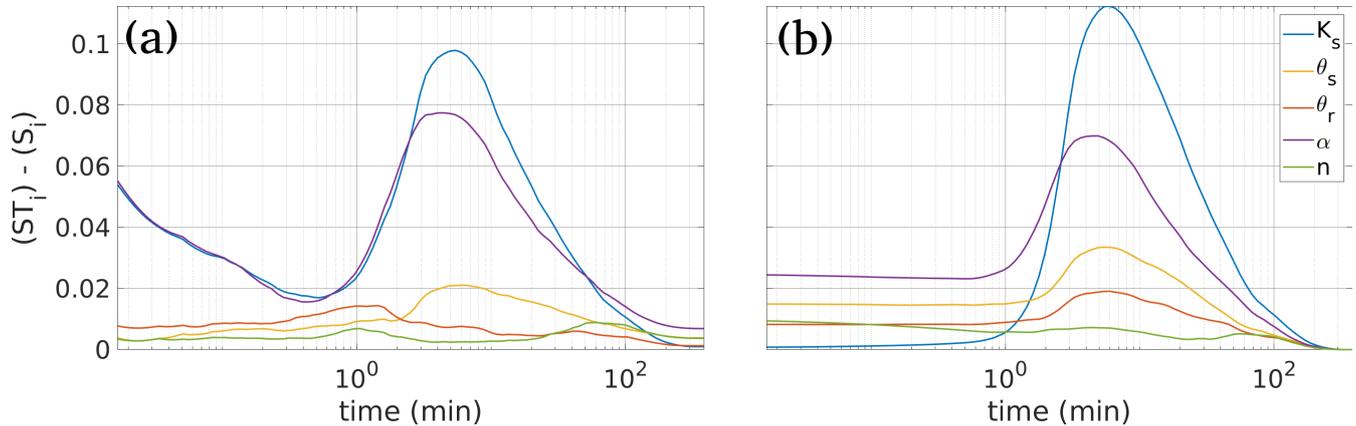
Figure 5. Difference between the total (ST_i) and the first order (S_i) sensitivity indices for all parameters for the TWT$_\mathrm{f}$ (a) and the TWT$_{120}$ (b) signals.

To evaluate further the effect of the unsaturated soil parameters on the TWT$_\mathrm{f}$, we plot the marginal effect of each parameter (Fig.6). The marginal effect can be easily derived from the PCE coefficients and reflects the effect of one parameter on the output signal. Fig.6 depicts the marginal effects of each hydraulic parameter, i.e. their influence on the TWT signals as a function of their value when they vary over the range of their prior distribution interval, while the other hydraulic parameters are kept fixed at their center value. This representation allows determining the regions of influence of the hydraulic parameters, given that the stronger the slope of the marginal effect curve, the higher the influence of the parameter. These marginal effects can vary over time, so we represent them at the three time steps ($t_1 = 1$ min, $t_2 = 5$ min, and $t_3 = 200$ min) highlighted with dotted vertical black lines in Fig.4. The oscillations are caused by numerical artifacts related to the degree of the polynomials used in the PCE model. From Fig.6a, it can be noticed that:

- K_s is highly influential at the beginning of the experiment. At $t_1 = 1$ min, the TWT$_\mathrm{f}$ signal varies almost linearly with K_s. Indeed, at the beginning of the experiment, when K_s increases, the wetting front is more advanced, thus, the GPR wave propagates at a lower speed and the TWT$_\mathrm{f}$ signal increases. At $t_2 = 5$ min, the TWT$_\mathrm{f}$ signal is sensitive only for small K_s values. Indeed, for high K_s values, the soil is fully saturated and the perturbation of the high value of K_s doesn't change the TWT$_\mathrm{f}$ signal. At $t_3 = 200$ min, the soil is fully saturated for almost all K_s values, thus, the TWT$_\mathrm{f}$ signal becomes insensitive to K_s.

- θ_s has no influence at the first times ($t_1 = 1$ min) since unsaturated conditions occur. For long times, the TWT$_\mathrm{f}$ signal is very sensitive to θ_s with an almost linear behavior. Indeed, when the soil is fully saturated, the dielectric permittivity and thus the TWT$_\mathrm{f}$ signal is almost proportional to θ_s.

- the sensitivity of TWT$_\mathrm{f}$ to θ_r is moderate and can be observed only at the beginning of the experiment (unsaturated conditions) with an almost linear behavior observable at $t = 1$ min and 5 min. The positive slope of the curve is consistent
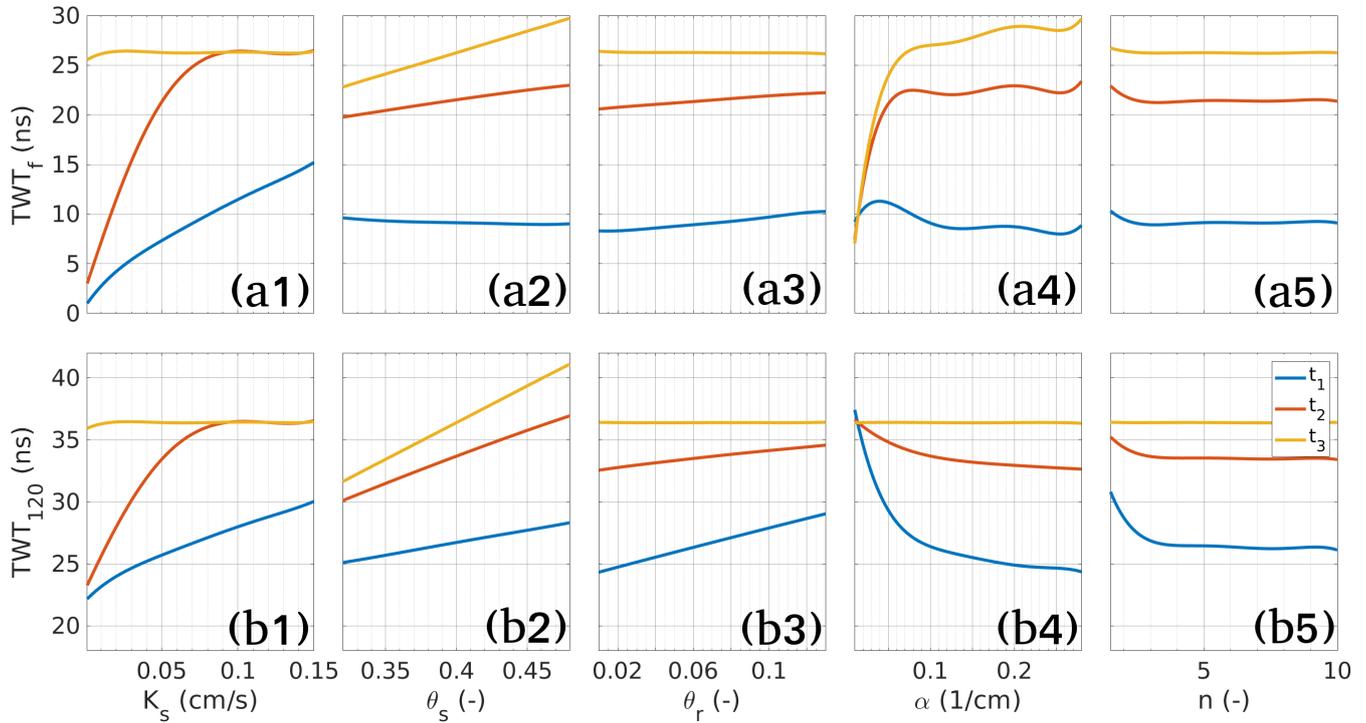
Figure 6. Marginal effects of the unsaturated soil parameters K_s, θ_s, θ_r, α and n on the TWT_f and TWT_{120} signals at three different times $t_1 = 1$ min, $t_2 = 5$ min, and $t_3 = 200$ min, highlighted in Fig.4.

with the physics of the process (when θ_r increases, the speed of the electromagnetic wave decreases, and the TWT_f signal increases).

– The van Genuchten parameter α is highly influential notably for long times ($t_3 = 200$ min). A small variation of the parameter α can induce a strong variation of the TWT_f signal. Notably, the sensitivity of α is very high for $\alpha \leq 0.05$ cm^{-1}.

– The sensitivity of TWT_f to the parameter n is almost zero (flat curves) at all times ($t = 1$ min, 5 min, and 200 min). The parameter n has therefore a negligible effect on the TWT_f signal and, as a consequence, it is expected to be poorly identifiable from the TWT_f data.

3.2.2   GSA of the TWT_{120} signal

The variance of the TWT_{120} signal is nonzero at the beginning of the experiment which means that the TWT_{120} signal is affected by the initial conditions (Fig.4c). Indeed, at the very beginning, the pressure distribution is hydrostatic and the water content distribution in the column is obtained from Eq.2 which depends on all soil parameters except K_s. Therefore, the speed of the GPR wave depends on the initial water content distribution which is dependent on the unsaturated soil parameters θ_s,

θ_r, α, and n. The most influential parameter at the beginning of the experiment is the parameter α. Over time, the effect of this parameter reduces, whereas the effect of θ_s increases. For long times, θ_s becomes the only sensitive parameter. The parameter K_s is also very sensitive. Its effect starts at zero, and increases until a maximum is reached at around 3 min, then it slowly decreases and becomes negligible after 100 min. As with the TWT$_f$ signal, interactions between parameters are moderate. The

300   difference between the total and first-order Sobol indices is negligible for all parameters except after 1 min for the parameters K_s, α and θ_s (see Fig.5b). This interaction corresponds to the blank region, between the variance curve and the shaded area in Fig.4c. The marginal effects of the soil parameters on the TWT$_{120}$ signal are plotted in Fig.6b for $t = 1$ min, 5 min, and 200 min. The curves in this figure show that:

- As for the TWT$_f$ signal, K_s is highly sensitive, especially for $t = 1$ min and 5 min.

305   - The saturated water content θ_s is very influential for all times. The TWT$_{120}$ varies almost linearly with θ_s even at the beginning ($t_1 = 1$ min), since the fixed reflector is located in the lower saturated region.

- As for the TWT$_f$ signal, θ_r is sensitive only at the beginning of the experiment (unsaturated conditions) with an almost linear behavior at $t = 1$ min and 5 min. When θ_r increases, the water content increases, and hence, the TWT$_{120}$ increases.

- The van Genuchten parameter α is highly sensitive. However, contrarily to the TWT$_f$ signal where α is highly sensitive
310   at long times ($t_3 = 200$ min), the sensitivity of α for the TWT$_{120}$ signal is high at short times ($t_1 = 1$ min). For long times, the influence of α disappears since the soil becomes fully saturated. The negative slope of the curve of the TWT$_{120}$ signal as a function of α observed at the beginning of the experiment is consistent with the physics of the process. Indeed, when α increases, the capillary fringe thickness decreases, hence, the water content in the unsaturated zone decreases, and thus the TWT$_{120}$ signal decreases.

315   - Surprisingly, and contrarily to the TWT$_f$ signal which showed a flat curve for the marginal effect of the parameter n for all parameter values and at all investigated times, the TWT$_{120}$ signal is sensitive to n at the beginning of the experiment ($t_1 = 1$ min) with a high sensitivity for $n < 3.5$ and a moderate sensitivity (the curve has a small slope) for $n \geq 3.5$.

4   Bayesian soil parameter estimation from the TWT signals

In this section, we estimate the unsaturated soil parameters in a Bayesian framework using the Markov Chain Monte Carlo
320   (MCMC) sampler (Vrugt and Bouten, 2002; Vrugt et al., 2008). The statistical calibration is performed for a GPR monitored infiltration experiment in order to address the following questions:

1. Can we obtain an appropriate estimation of all unsaturated soil parameters from TWT data?

2. What is the impact of the kind of TWT data (moving/fixed reflectors) and of the number of reflectors on the calibrated model parameters and their confidence intervals?

325   3. What is the optimal set of TWT measurements that yields good reliability of all unsaturated soil parameters?

The MCMC method has been successfully employed in various inverse hydrological problems (e.g., Fajraoui et al., 2011; Younes et al., 2016; Younes et al., 2017; Younes et al., 2018). The method generates random sequences of parameter sets that asymptotically converge toward the target joint posterior distribution by searching the ensemble of possible parameter sets that satisfactorily fit the observations. The converged sets can then be used to assess the quality of the parameter estimation

330   such as the optimal parameter values and the 95% Confidence Intervals (CIs) which allow for evaluating the reliability of the parameters via uncertainty quantification.

In the sequel, the MCMC method is performed with the DREAM$_{(ZS)}$ software (Laloy and Vrugt, 2012), which is an efficient MCMC sampler. The vector of unknowns is formed by the five unsaturated soil parameters (K_s, θ_s, θ_r, α, n). A reference solution is generated by simulating the hydrogeophysical problem formed by the system of equations (1)-(6) using the following

335   reference parameter values $K_s^* = 0.08$ cm/s, $\theta_s^* = 0.4$, $\theta_r^* = 0.07$, $\alpha^* = 0.145$ cm^{-1}, $n^* = 2.68$, as shown in Table 3. The TWT$_f$, TWT$_{50}$, and TWT$_{120}$ signals used as calibration data are deduced from the results of the simulation using the reference parameter values. These TWT signals are then independently corrupted using a normally distributed noise with a standard deviation $\sigma = 0.5$ ns.

The TWT$_f$, TWT$_{50}$ and TWT$_{120}$ calibration signals, illustrated before noise corruption in Fig.2, increase almost linearly until

340   reaching a plateau. For the TWT$_{50}$ signal, the plateau is reached when the infiltration front attains the R50 reflector and the value of the plateau corresponds to the time needed by the electromagnetic wave to make a round trip from the surface to a 50 cm depth of a full saturated porous medium. For the TWT$_{120}$ signal, the plateau signal is reached when the infiltration front attains the water table (the domain becomes fully saturated) and the value of the plateau corresponds to the time needed by the electromagnetic wave to make a round trip from the surface to a 120 cm deep of a fully saturated porous medium. For TWT$_f$,

345   the plateau value is also reached when the infiltration front attains the water table and the value of the plateau corresponds to the time needed by the electromagnetic wave to make a round trip from the surface to the water table at 100 cm deep.

The reliability of the unsaturated soil parameters is assessed for 5 different scenarios of measurement sets. In the first scenario, only data of the wetting-front TWT$_f$ signal are used for the calibration. The second and third scenarios use only the TWT$_{50}$ and TWT$_{120}$ signal, respectively, obtained from reflection on the fixed reflector R50 and R120. The fourth scenario

350   uses both data of TWT$_f$ and TWT$_{120}$ as fitting data. The last scenario investigates the benefit of adding a fixed reflector by using data of the TWT$_f$, TWT$_{50}$ and TWT$_{120}$ signals as conditioning information.

In the five scenarios, the MCMC sampler uses three parallel chains and a total number of 50000 runs. The last 25% of the runs that adequately fit the model onto observations are used to estimate the joint posterior distribution.

The MCMC results of the five studied scenarios are given in Table 3 which depicts, for each parameter, the mean estimated

355   value, its posterior CI size, and the ratio of prior to posterior intervals. Note that the CI and the last indicator are calculated from the standard deviation by assuming a Gaussian posterior distribution. A small CI indicates an accurate estimation of the parameter. A significant difference between the prior and posterior intervals is a sign of the high sensitivity of the model to that parameter (Dusek et al., 2015).

Results of table 3 for scenario 1 using only data of the TWT$_f$ signal for the estimation of the unsaturated soil parameters

360   show that:

	K_s (cm/s)	θ_s (-)	θ_r (-)	α (1/cm)	n (-)
$\boldsymbol{X}^*$	0.08	0.40	0.07	0.145	2.68
Scenario 1	**0.081**	**0.39**	**0.076**	**0.211**	**2.75**
TWT_f	(0.037)	(0.031)	(0.14)	(0.167)	(0.93)
	4	*5*	*1*	*2*	*9*
Scenario 2	**0.074**	**0.4**	**0.081**	**0.173**	**5.79**
TWT_{50}	(0.023)	(0.008)	(0.061)	(0.269)	(9.99)
	6	*19*	*2*	*1*	*1*
Scenario 3	**0.078**	**0.4**	**0.089**	**0.167**	**5.93**
TWT_{120}	(0.011)	(0.007)	(0.053)	(0.195)	(9.36)
	13	*24*	*2*	*1*	*1*
Scenario 4	**0.08**	**0.4**	**0.074**	**0.151**	**2.72**
$\text{TWT}_f,$	(0.003)	(0.004)	(0.015)	(0.029)	(0.5)
TWT_{120}	*46*	*37*	*8*	*9*	*17*
Scenario 5	**0.079**	**0.4**	**0.073**	**0.149**	**2.68**
$\text{TWT}_f,$	(0.003)	(0.004)	(0.015)	(0.027)	(0.49)
$\text{TWT}_{50},$	*49*	*44*	*8*	*10*	*17*
TWT_{120}					

Table 3. First line: Reference values used to build the synthetic calibration data. Then for the different scenarios: estimated mean values (bold), size of the posterior confidence intervals (CIs) (between brackets), and ratio of prior to posterior intervals (italic).

- An accurate estimation of K_s, the most sensitive parameter (Fig.4a), is obtained with a CI of 0.037 cm/s and a variation interval reduced by 4.

- A fair estimate of the parameters θ_s with a standard deviation of 0.031 (-) and a reduction of the interval of variation by 5. This result is relatively surprising as this parameter did not show a strong influence on TWT_f sensitivity (Fig.4a).

365   - The parameter θ_r is not well estimated. Indeed, although its mean estimated value is very close to its reference value, the associated uncertainty of 0.14 is large and the posterior interval is as large as the prior one, which indicates the low reliability of the estimation.

- A poor estimation of α, while the sensitivity analysis showed it has a strong influence on TWT_f (Fig.4a). Its CI is large, with a value of 0.167 cm^{-1} and its posterior interval size is half the prior one.

370   – The TWT$_f$ signal yields a mean estimated value $n = 2.75 \pm 0.47$ which is close to the reference value $n^* = 2.68$. The parameter n is quite well identified since its posterior interval is 9 times smaller than the prior interval. This is relatively surprising since the sensitivity of n is negligible (Fig.4a and 6a5).

In summary, using only data of the TWT$_f$ signal as conditioning information for the hydrogeophysical model calibration yielded well mean estimated parameter values, close to the reference values for all unsaturated soil parameters. However, the

375   examination of the associated uncertainties, showed that only K_s, θ_s, and n are correctly identified (with narrow posterior intervals with respect to the prior ones). This points out the importance of statistical calibration methods for highly nonlinear problems to investigate not only estimated parameter values but also the associated uncertainties.

The estimation of the unsaturated soil parameters for scenarios 2 and 3, using only data of the TWT$_{50}$ or TWT$_{120}$ signal for the calibration shows that:

380   – The parameters K_s and θ_s, which are the most sensitive parameters during most of the experiment (Fig.4b and 4c), are well identified with small CI size and strong reductions by at least 6 for K_s, and 19 for θ_s, of their intervals of variation. We note that the TWT$_{120}$ signal allows a much better estimate of both K_s and θ_s as their CIs are smaller than the ones estimated with TWT$_{50}$. It is especially true for K_s where there is almost a factor 2 between the reduction ratios.

       – The soil parameters θ_r, α, and n, although sensitive (Fig.4b and 4c), cannot be identified from the TWT$_{50}$ and TWT$_{120}$

385   signals since their posterior intervals are as large as, or at best two times smaller than their prior ones.

The results of scenario 4 which combines data of TWT$_f$ and TWT$_{120}$ signals show that:

       – Both parameters K_s, θ_s, and n are very well identified, with very narrow posterior intervals showing a strong reduction by 46, 37, and 17 of their prior intervals, respectively.

       – The parameters θ_r and α are reasonably well estimated with mean values very close to their reference and intervals of

390   variation reduced by 8 and 9, respectively.

Finally, the results of the last scenario which combines data of TWT$_f$, TWT$_{50}$ and TWT$_{120}$ signals, show performances very similar to scenario 4. Additional information from TWT$_{50}$ helped to reduce slightly the posterior intervals of K_s, θ_s, and α that in that case show a reduction of 49, 44, and 10 times their prior intervals, respectively.

The results of MCMC for this last scenario are shown in Fig.7 where diagonal plots depict the inferred posterior parameter

395   distributions and the off-diagonal scatterplots represent the pairwise correlations in the MCMC draws. Almost bell-shaped posterior distributions are obtained for all unsaturated soil parameters. Negligible correlations are observed between the parameters, except moderate correlations observed between K_s and θ_r (r=-0.78) and between n and θ_r (r=0.64) .

Note that the parameter n is relatively well estimated as the target reference value 2.68 is located in the high sensitivity region ($n < 3.5$) (Fig.6). In the case of a reference value located in the low sensitivity region ($n \geq 3.5$), the calibration of the

400   hydrogeophysical model using TWT$_f$ and TWT$_{120}$ signals yields a much poorer identification of the parameter n. For instance,
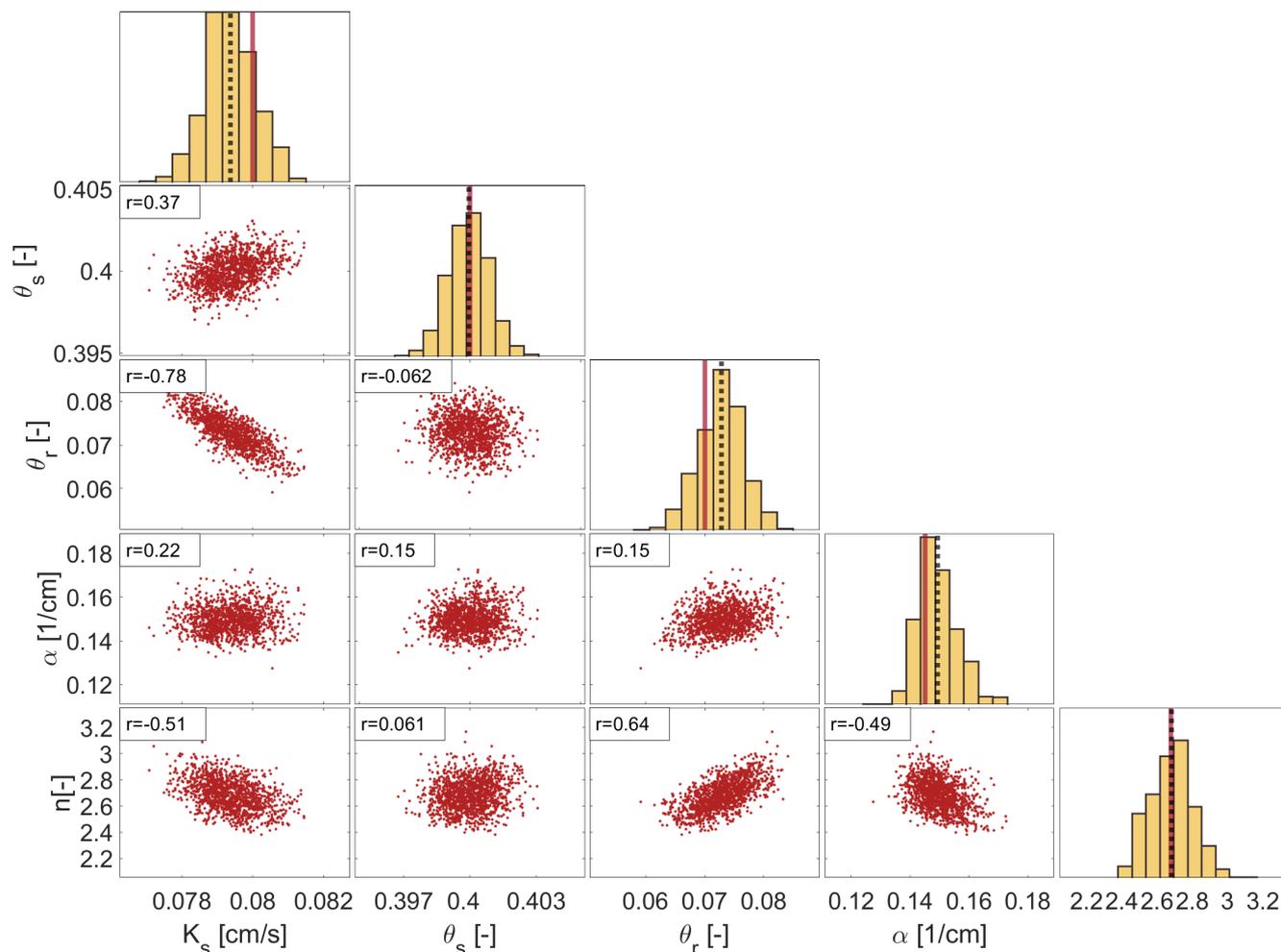
Figure 7. MCMC solutions using TWT_f, TWT_{50} and TWT_{120} signals for the calibration of the hydrogeophysical model. The diagonal plots represent the inferred posterior parameter distributions, showing the estimated mean value (dotted black line) and the target value (hard red line). The off-diagonal represents the pairwise correlations between parameters.

using scenario 5 with a reference value $n^* = 4.25$, the estimated mean value is 4.84 with a posterior CI size of 3.6, which corresponds to a reduction of the interval of variation by only 2.

These results point to the high benefit, for the identification of the unsaturated soil parameters, of combining the GPR signal data of a fixed reflector, preferably located sufficiently deep in the soil, with the TWT signal of the moving infiltration wetting front. This combination allows good reliability of almost all soil parameters with very narrow posterior intervals in comparison with the prior ones. In particular, the van Genuchten parameter n is relatively well identified for investigated sandy soil where $n < 3.5$.

5   Conclusions

In this work, we investigated the interest in ground penetrating radar (GPR) time data for the estimation of hydrodynamic
410   unsaturated soil parameters. To this aim, water infiltration into an initially unsaturated sandy soil has been simulated using a
one-dimensional hydrogeophysical model. GPR time signals have been analyzed from the reflection of the electromagnetic
wave on the moving wetting front and on two fixed reflectors located at different depths. GSA, based on PCE decomposition,
has been used to assess the effect of the unsaturated soil parameters (saturated hydraulic conductivity, saturated and residual
water contents, and Mualem–van Genuchten shape parameters α and n) on the different TWT signals. Statistical calibration of
415   the unsaturated soil parameters has been performed with the MCMC sampler using corrupted synthetic observations to evaluate
the reliability of the soil parameters from the TWT signals.

The results of GSA showed that the $\mathrm{TWT_f}$ signal of the wetting front is different from that of the two fixed reflectors which
had similar behavior. For the fixed reflectors, the magnitude of the variance (and therefore the sensitivity of the soil parameters)
is more pronounced for deeper reflectors. The $\mathrm{TWT_f}$ signal is highly sensitive to K_s and α and moderately sensitive to θ_s. A
420   low sensitivity was observed for θ_r, whereas the parameter n was insensitive. The $\mathrm{TWT_{120}}$ signal of the fixed reflector located
at 120 cm depth is highly sensitive to K_s, θ_s and α, and moderately sensitive to θ_r. The van Genuchten parameter n has a high
sensitivity for $n < 3.5$ and a poor sensitivity for $n \geq 3.5$.

The reliability of the unsaturated soil parameters has been assessed for 5 different scenarios of TWT measurement sets.
When only data of the $\mathrm{TWT_f}$ signal are used as conditioning information for the model calibration, all estimated parameter
425   values were very close to the reference values. However, analyzing the associated uncertainties showed that only K_s, θ_s, and
n were correctly identified (with narrow posterior intervals). Further, using only data of the $\mathrm{TWT_{50}}$ or $\mathrm{TWT_{120}}$ signals for the
calibration allows also only a good identification of K_s and θ_s with a strong reduction of their intervals of variation. The best
results, in terms of parameter reliability, are obtained with the combination of $\mathrm{TWT_f}$ with fixed reflectors. In this case, the
four parameters K_s, θ_s, θ_r, and α are very well identified with very narrow posterior interval. The van Genuchten parameter
430   n is estimated with a low uncertainty but its estimation degrades in the low sensitivity region $n \geq 3.5$. We note that the deeper
reflectors provide more information as the inversion of its signal furnishes parameters with lower uncertainty. Then using two
or three reflectors in addition to the wetting front signal doesn't reduce consequently the uncertainty of the parameters.

The results of this study highlight the high benefit of combining TWT signals of fixed and moving (infiltration wetting front)
reflectors for very good identification of all the unsaturated soil parameters. It also points out the role of GSA to assess the
435   influence of the parameters on the output signals and the necessity to perform statistical calibration to assess the reliability of
model parameters by evaluating not only estimated parameter values but also their associated uncertainties.

Acknowledgements

The doctoral position of the first author is co-funded by the Grand-Est Region and the University of Strasbourg. This research
work is partly funded by the French National Research Agency through the Exciting project ANR-17-CE06-0012-01. Finally,
440   computing time was provided by the HPC-UdS.

Code availability. The hydrological code WAMOS-1D, the coupled hydrogeophysical model, and the global sensitivity analysis tools can be provided upon request by the authors.

Data availability. All data presented in this paper is available upon request from the authors.

Author contributions. GJF and LN formulated the aims of the research. BB, LF, and YA provided the hydrological code. YA provided
445 the resources for sensitivity analysis and Bayesian estimation studies. MR established the hydrogeophysical coupled model and ran all experiments under the supervision of GJF and LN, and validation of all co-authors. MR prepared the manuscript with reviewing and editing contributions from all co-authors.

Competing interests. The authors declare that they have no conflict of interest.

Acknowledgements. The doctoral position of the first author is co-funded by the Grand-Est Region and the University of Strasbourg. This
450 research work is partly funded by the French National Research Agency through the Exciting project ANR-17-CE06-0012-01. The authors would like to acknowledge the High-Performance Computing Center of the University of Strasbourg for supporting this work by providing scientific support and access to computing resources. Part of the computing resources was funded by the Equipex Equip@Meso project (Programme Investissements d'Avenir) and the CPER Alsacalcul/Big Data.

References

455   Annan, P.: Ground penetrating radar: Principles, procedures and applications, Sensors and Software Inc, 2003.

Bano, M.: Effects of the transition zone above a water table on the reflection of GPR waves, Geophysical Research Letters, 33, https://doi.org/https://doi.org/10.1029/2006GL026158, 2006.

Belfort, B., Toloni, I., Ackerer, P., Cotel, S., Viville, D., and Lehmann, F.: Vadose Zone Modeling in a Small Forested Catchment: Impact of Water Pressure Head Sampling Frequency on 1D-Model Calibration, Geosciences, 8, https://doi.org/10.3390/geosciences8020072, 2018.

460   Belfort, B., Weill, S., Fahs, M., and Lehmann, F.: Laboratory Experiments of Drainage, Imbibition and Infiltration under Artificial Rainfall Characterized by Image Analysis Method and Numerical Simulations, Water, 11, https://doi.org/10.3390/w11112232, 2019.

Binley, A., Hubbard, S. S., Huisman, J. A., Revil, A., Robinson, D. A., Singha, K., and Slater, L. D.: The emergence of hydro-geophysics for improved understanding of subsurface processes over multiple scales, Water Resources Research, 51, 3837–3866, https://doi.org/https://doi.org/10.1002/2015WR017016, 2015.

465   Birchak, J., Gardner, C., Hipp, J., and Victor, J.: High dielectric constant microwave probes for sensing soil moisture, Proceedings of the IEEE, 62, 93–98, https://doi.org/10.1109/PROC.1974.9388, 1974.

Busch, S., Weihermüller, L., Huisman, J. A., Steelman, C. M., Endres, A. L., Vereecken, H., and van der Kruk, J.: Coupled hydrogeophysical inversion of time-lapse surface GPR data to estimate hydraulic properties of a layered subsurface, Water Resources Research, 49, 8480–8494, https://doi.org/https://doi.org/10.1002/2013WR013992, 2013.

470   Costabel, S. and Günther, T.: Noninvasive Estimation of Water Retention Parameters by Observing the Capillary Fringe with Magnetic Resonance Sounding, Vadose Zone Journal, 13, vzj2013.09.0163, https://doi.org/https://doi.org/10.2136/vzj2013.09.0163, 2014.

Dal Bo, I., Klotzsche, A., Schaller, M., Ehlers, T. A., Kaufmann, M. S., Fuentes Espoz, J. P., Vereecken, H., and van der Kruk, J.: Geophysical imaging of regolith in landscapes along a climate and vegetation gradient in the Chilean coastal cordillera, CATENA, 180, 146–159, https://doi.org/https://doi.org/10.1016/j.catena.2019.04.023, 2019.

475   de Jong, S. M., Heijenk, R. A., Nijland, W., and van der Meijde, M.: Monitoring Soil Moisture Dynamics Using Electrical Resistivity Tomography under Homogeneous Field Conditions, Sensors, 20, https://doi.org/10.3390/s20185313, 2020.

Doolittle, J. A. and Brevik, E. C.: The use of electromagnetic induction techniques in soils studies, Geoderma, 223-225, 33–45, https://doi.org/https://doi.org/10.1016/j.geoderma.2014.01.027, 2014.

Dusek, J., Dohnal, M., Snehota, M., Sobotkova, M., Ray, C., and Vogel, T.: Transport of bromide and pesticides through an undis-
480   turbed soil column: A modeling study with global optimization analysis, Journal of Contaminant Hydrology, 175-176, 1–16, https://doi.org/https://doi.org/10.1016/j.jconhyd.2015.02.002, 2015.

Edemsky, D., Popov, A., Prokopovich, I., and Garbatsevich, V.: Airborne Ground Penetrating Radar, Field Test, Remote Sensing, 13, https://doi.org/10.3390/rs13040667, 2021.

Fajraoui, N., Ramasomanana, F., Younes, A., Mara, T. A., Ackerer, P., and Guadagnini, A.: Use of global sensitivity analysis and polynomial
485   chaos expansion for interpretation of nonreactive transport experiments in laboratory-scale porous media, Water Resources Research, 47, https://doi.org/https://doi.org/10.1029/2010WR009639, 2011.

Huisman, J. A., Hubbard, S. S., Redman, J. D., and Annan, A. P.: Measuring Soil Water Content with Ground Penetrating Radar: A Review, Vadose Zone Journal, 2, 476–491, https://doi.org/https://doi.org/10.2136/vzj2003.4760, 2003.

Jadoon, K. Z., Weihermüller, L., Scharnagl, B., Kowalsky, M. B., Bechtold, M., Hubbard, S. S., Vereecken, H., and Lambot, S.: Estimation of Soil Hydraulic Parameters in the Field by Integrated Hydrogeophysical Inversion of Time-Lapse Ground-Penetrating Radar Data, Vadose Zone Journal, 11, vzj2011.0177, https://doi.org/https://doi.org/10.2136/vzj2011.0177, 2012.

Jaumann, S. and Roth, K.: Soil hydraulic material properties and layered architecture from time-lapse GPR, Hydrology and Earth System Sciences, 22, 2551–2573, https://doi.org/10.5194/hess-22-2551-2018, 2018.

Jonard, F., Weihermüller, L., Schwank, M., Jadoon, K. Z., Vereecken, H., and Lambot, S.: Estimation of Hydraulic Properties of a Sandy Soil Using Ground-Based Active and Passive Microwave Remote Sensing, IEEE Transactions on Geoscience and Remote Sensing, 53, 3095–3109, https://doi.org/10.1109/TGRS.2014.2368831, 2015.

Jones, S. B., Blonquist Jr., J. M., Robinson, D. A., Rasmussen, V. P., and Or, D.: Standardizing Characterization of Electromagnetic Water Content Sensors: Part 1. Methodology, Vadose Zone Journal, 4, 1048–1058, https://doi.org/https://doi.org/10.2136/vzj2004.0140, 2005.

Klotzsche, A., Jonard, F., Looms, M., van der Kruk, J., and Huisman, J.: Measuring Soil Water Content with Ground Penetrating Radar: A Decade of Progress, Vadose Zone Journal, 17, 180 052, https://doi.org/https://doi.org/10.2136/vzj2018.03.0052, 2018.

Laloy, E. and Vrugt, J. A.: High-dimensional posterior exploration of hydrologic models using multiple-try DREAM(ZS) and high-performance computing, Water Resources Research, 48, https://doi.org/https://doi.org/10.1029/2011WR010608, 2012.

Léger, E., Saintenoy, A., and Coquet, Y.: Hydrodynamic parameters of a sandy soil determined by ground-penetrating radar inside a single ring infiltrometer, Water Resources Research, 50, 5459–5474, https://doi.org/https://doi.org/10.1002/2013WR014226, 2014.

Léger, E., Saintenoy, A., Tucholka, P., and Coquet, Y.: Hydrodynamic Parameters of a Sandy Soil Determined by Ground-Penetrating Radar Monitoring of Porchet Infiltrations, IEEE Journal of Selected Topics in Applied Earth Observations and Remote Sensing, 9, 188–200, https://doi.org/10.1109/JSTARS.2015.2464231, 2016.

Léger, E., Saintenoy, A., Coquet, Y., Tucholka, P., and Zeyen, H.: Evaluating hydrodynamic parameters accounting for water retention hysteresis in a large sand column using surface GPR, Journal of Applied Geophysics, 182, 104 176, https://doi.org/https://doi.org/10.1016/j.jappgeo.2020.104176, 2020.

Mara, T. and Tarantola, S.: Application of Global Sensitivity Analysis of Model Output to Building Thermal Simulations, Building Simulation, 1, 290–302, https://doi.org/10.1007/s12273-008-8129-5, 2008.

Moysey, S. M.: Hydrologic trajectories in transient ground-penetrating-radar reflection data, GEOPHYSICS, 75, WA211–WA219, https://doi.org/10.1190/1.3463416, 2010.

Mualem, Y.: A new model for predicting the hydraulic conductivity of unsaturated porous media, Water Resources Research, 12, 513–522, https://doi.org/https://doi.org/10.1029/WR012i003p00513, 1976.

Richards, L. A.: CAPILLARY CONDUCTION OF LIQUIDS THROUGH POROUS MEDIUMS, Physics, 1, 318–333, https://doi.org/10.1063/1.1745010, 1931.

Robinson, D. A., Campbell, C. S., Hopmans, J. W., Hornbuckle, B. K., Jones, S. B., Knight, R., Ogden, F., Selker, J., and Wendroth, O.: Soil Moisture Measurement for Ecological and Hydrological Watershed-Scale Observatories: A Review, Vadose Zone Journal, 7, 358–389, https://doi.org/https://doi.org/10.2136/vzj2007.0143, 2008.

Saintenoy, A. and Hopmans, J. W.: Ground Penetrating Radar: Water Table Detection Sensitivity to Soil Water Retention Properties, IEEE Journal of Selected Topics in Applied Earth Observations and Remote Sensing, 4, 748–753, https://doi.org/10.1109/JSTARS.2011.2171920, 2011.

Saintenoy, A., Schneider, S., and Tucholka, P.: Evaluating Ground-Penetrating Radar use for water infiltration monitoring, Vadose Zone Journal, 7, 208–214, https://hal.archives-ouvertes.fr/hal-00831408, 2008.

Saito, H., Kuroda, S., Iwasaki, T., Fujimaki, H., Nagai, N., and Sala, J.: Tracking Infiltration Front Depth Using Time-lapse Multi-offset Gathers Collected with Array Antenna Ground Penetrating Radar, Journal of Visualized Experiments, 2018, https://doi.org/10.3791/56847, 2018.

530 Scharnagl, B., Vrugt, J. A., Vereecken, H., and Herbst, M.: Inverse modelling of in situ soil water dynamics: investigating the effect of different prior distributions of the soil hydraulic parameters, Hydrology and Earth System Sciences, 15, 3043–3059, https://doi.org/10.5194/hess-15-3043-2011, 2011.

Scholer, M., Irving, J., Binley, A., and Holliger, K.: Estimating vadose zone hydraulic properties using ground penetrating radar: The impact of prior information, Water Resources Research, 47, https://doi.org/https://doi.org/10.1029/2011WR010409, 2011.

535 Shao, Q., Younes, A., Fahs, M., and Mara, T. A.: Bayesian sparse polynomial chaos expansion for global sensitivity analysis, Computer Methods in Applied Mechanics and Engineering, 318, 474–496, https://doi.org/https://doi.org/10.1016/j.cma.2017.01.033, 2017.

Sobol′, I.: Global sensitivity indices for nonlinear mathematical models and their Monte Carlo estimates, Mathematics and Computers in Simulation, 55, 271–280, https://doi.org/https://doi.org/10.1016/S0378-4754(00)00270-6, the Second IMACS Seminar on Monte Carlo Methods, 2001.

540 van Genuchten, M. T.: A Closed-form Equation for Predicting the Hydraulic Conductivity of Unsaturated Soils, Soil Science Society of America Journal, 44, 892–898, https://doi.org/https://doi.org/10.2136/sssaj1980.03615995004400050002x, 1980.

Vereecken, H., Huisman, J., Bogena, H., Vanderborght, J., Vrugt, J., Hopmans, J., and Vereecken, C.: On the value of soil moisture measurements in vadose zone hydrology: A review, Water Resources Research - WATER RESOUR RES, 44, https://doi.org/10.1029/2008WR006829, 2008.

545 Vrugt, J. A. and Bouten, W.: Validity of First-Order Approximations to Describe Parameter Uncertainty in Soil Hydrologic Models, Soil Science Society of America Journal, 66, 1740–1751, https://doi.org/https://doi.org/10.2136/sssaj2002.1740, 2002.

Vrugt, J. A., Stauffer, P. H., Wöhling, T., Robinson, B. A., and Vesselinov, V. V.: Inverse Modeling of Subsurface Flow and Transport Properties: A Review with New Developments, Vadose Zone Journal, 7, 843–864, https://doi.org/https://doi.org/10.2136/vzj2007.0078, 2008.

550 Wiener, N.: The Homogeneous Chaos, American Journal of Mathematics, 60, 897–936, http://www.jstor.org/stable/2371268, 1938.

Younes, A., Mara, T. A., Fajraoui, N., Lehmann, F., Belfort, B., and Beydoun, H.: Use of Global Sensitivity Analysis to Help Assess Unsaturated Soil Hydraulic Parameters, Vadose Zone Journal, 12, vzj2011.0150, https://doi.org/https://doi.org/10.2136/vzj2011.0150, 2013.

Younes, A., Delay, F., Fajraoui, N., Fahs, M., and Mara, T.: Global sensitivity analysis and Bayesian parameter in-
555 ference for solute transport in porous media colonized by biofilms, Journal of Contaminant Hydrology, 191, 1–18, https://doi.org/https://doi.org/10.1016/j.jconhyd.2016.04.007, 2016.

Younes, A., Mara, T., Fahs, M., Olivier, G., and Ackerer, P.: Hydraulic and transport parameter assessment using column infiltration experiments, Hydrology and Earth System Sciences, 21, 2263–2275, https://doi.org/10.5194/hess-21-2263-2017, 2017.

Younes, A., Zaouali, J., Lehmann, F., and Fahs, M.: Sensitivity and identifiability of hydraulic and geophysical parameters from streaming
560 potential signals in unsaturated porous media, Hydrology and Earth System Sciences, 22, 3561–3574, https://doi.org/10.5194/hess-22-3561-2018, 2018.

Zhang, L., Niu, Y., Zhang, H., Han, W., Guang, L., and Xingshuo, P.: Maize Canopy Temperature Extracted From UAV Thermal and RGB Imagery and Its Application in Water Stress Monitoring, Frontiers in Plant Science, 10, https://doi.org/10.3389/fpls.2019.01270, 2019.